LOFAR discovery of a double radio halo system in Abell 1758 and radio/X-ray study of the cluster pair

Botteon, A.; Shimwell, T.W.; Bonafede, A.; Dallacasa, D.; Brunetti, G.; Mandal, S.; ... ; Venturi, T.

LOFAR discovery of a double radio halo system in Abell 1758 and radio/X-ray study of the cluster pair

A. Botteon[1,2]*, T. W. Shimwell[3,4], A. Bonafede[1,2,5], D. Dallacasa[1,2], G. Brunetti[2],
S. Mandal[4], R. J. van Weeren[4], M. Brüggen[5], R. Cassano[2], F. de Gasperin[4],
D. N. Hoang[4], M. Hoeft[6], H. J. A. Röttgering[4], F. Savini[5], G. J. White[7,8],
A. Wilber[5] and T. Venturi[2]

[1]*Dipartimento di Fisica e Astronomia, Università di Bologna, via P. Gobetti 93/2, I-40129 Bologna, Italy*
[2]*INAF - IRA, via P. Gobetti 101, I-40129 Bologna, Italy*
[3]*ASTRON, the Netherlands Institute for Radio Astronomy, Postbus 2, NL-7990 AA Dwingeloo, The Netherlands*
[4]*Leiden Observatory, Leiden University, PO Box 9513, NL-2300 RA Leiden, The Netherlands*
[5]*Hamburger Sternwarte, Universität Hamburg, Gojenbergsweg 112, D-21029 Hamburg, Germany*
[6]*Thüringer Landessternwarte, Sternwarte 5, D-07778 Tautenburg, Germany*
[7]*Department of Physical Sciences, The Open University, Milton Keynes MK7 6AA, England*
[8]*Space Science and Technology Department, The Rutherford Appleton Laboratory, Chilton, Didcot, Oxfordshire OX11 0NL*

ABSTRACT

Radio halos and radio relics are diffuse synchrotron sources that extend over Mpc-scales and are found in a number of merger galaxy clusters. They are believed to form as a consequence of the energy that is dissipated by turbulence and shocks in the intra-cluster medium (ICM). However, the precise physical processes that generate these steep synchrotron spectrum sources are still poorly constrained. We present a new LOFAR observation of the double galaxy cluster Abell 1758. This system is composed of A1758N, a massive cluster hosting a known giant radio halo, and A1758S, which is a less massive cluster whose diffuse radio emission is confirmed here for the first time. Our observations have revealed a radio halo and a candidate radio relic in A1758S, and a suggestion of emission along the bridge connecting the two systems which deserves confirmation. We combined the LOFAR data with archival VLA and GMRT observations to constrain the spectral properties of the diffuse emission. We also analyzed a deep archival *Chandra* observation and used this to provide evidence that A1758N and A1758S are in a pre-merger phase. The ICM temperature across the bridge that connects the two systems shows a jump which might indicate the presence of a transversal shock generated in the initial stage of the merger.

Key words: radio continuum: general – radiation mechanisms: non-thermal – radiation mechanisms: thermal – galaxies: clusters: individual: A1758 – galaxies: clusters: intracluster medium – X-rays: galaxies: clusters

1 INTRODUCTION

Diffuse and low surface brightness radio emission with steep spectrum ($\alpha > 1$, with $S_\nu \propto \nu^{-\alpha}$) associated with the intra-cluster medium (ICM) has been found in a number of merging galaxy clusters (see Feretti et al. 2012, for an overview). This emission, generally referred to as radio halos or radio relics, probes the synchrotron radiation from $\sim$ GeV relativistic electrons in the $\sim \mu$G cluster-scale magnetic fields.

Over the last two decades, important steps forward have been made in understanding the origin of non-thermal phenomena in the ICM. A milestone in this framework was the connection between diffuse radio emission in the ICM and dynamically disturbed systems (e.g. Buote 2001; Cassano et al. 2010b, 2013; Cuciti et al. 2015). This suggests that cluster mergers play a crucial role in the formation of halos and relics. During mergers, turbulence and shocks are generated in the ICM where they dissipate energy. A small fraction of this energy goes into the re-acceleration of relativistic particles and the amplification of the magnetic field (see Brunetti & Jones 2014, for a review).

In particular, giant radio halos are thought to be gener-

ated by (primary or secondary) electrons re-accelerated by turbulent-driven mechanisms during mergers (e.g. Petrosian 2001; Brunetti et al. 2001, 2007; Brunetti & Lazarian 2011, 2016; Pinzke, Oh & Pfrommer 2017; Brunetti, Zimmer & Zandanel 2017), although many aspects of the physics of these mechanisms remain poorly understood (see Brunetti 2016). Radio relics are thought to be generated by electrons accelerated or re-accelerated by shocks (e.g. Enßlin et al. 1998; Roettiger, Burns & Stone 1999; Hoeft & Brüggen 2007; Kang & Ryu 2011, 2016; Kang, Ryu & Jones 2012; Pinzke, Oh & Pfrommer 2013). Whilst a connection between radio relics and merger shocks is fairly well established (e.g. Macario et al. 2011; Akamatsu & Kawahara 2013; Botteon et al. 2016b), open problems include the efficiency of particle acceleration and the proton-to-electron ratio in the acceleration (e.g. Vazza & Brüggen 2014; Vazza et al. 2015a, 2016; Kang et al. 2014; Guo, Sironi & Narayan 2014a,b; Wittor, Vazza & Brüggen 2017). Shock re-acceleration for radio relics is an emerging scenario that seems to be supported by recent observations of clusters where radio galaxies located close to the relic position can provide seed electrons that are more easily re-accelerated by low Mach number shocks. This alleviates the large requirements of acceleration efficiencies (Bonafede et al. 2014; Shimwell et al. 2015; Botteon et al. 2016a; van Weeren et al. 2017).

The LOw Frequency ARray (LOFAR; van Haarlem et al. 2013) is a radio interferometer observing in the range between 10 and 90 MHz with Low Band Antennas (LBA) and between 110 and 240 MHz with High Band Antennas (HBA). It has long been recognized that LOFAR has the potential to make breakthroughs in the field of galaxy cluster science (e.g. Röttgering et al. 2006, 2011; Cassano et al. 2010a; Nuza et al. 2012). The high resolution allows for the structures of halos and relics to be precisely characterized and isolated from the often severe contamination from other radio emitting sources in the vicinity. The dense core provides excellent surface brightness sensitivity, that coupled with the low observing frequencies allows for sensitive observations.

The LOFAR Two-meter Sky Survey (LoTSS; Shimwell et al. 2017) is designed to fully exploit the potential of LOFAR and produce high resolution ($\sim 5''$) and high sensitivity (~ 100 μJy beam^{-1}) images of the entire northern sky at $120 - 168$ MHz. As part of this survey we have observed the double galaxy cluster Abell 1758. In this paper, we present this new LOFAR observation together with archival Giant Metrewave Radio Telescope (GMRT), Very Large Array (VLA) and *Chandra* data. Using these data we have discovered and characterized the second double radio halo system known to date and we argue that the two clusters that constitute Abell 1758 are in a pre-merger state.

Throughout this paper, we assume a ΛCDM cosmology with $\Omega_\Lambda = 0.7$, $\Omega_m = 0.3$ and $H_0 = 70$ km s^{-1} Mpc^{-1}. At the cluster redshift ($z = 0.279$) this corresponds to a luminosity distance of $D_L = 1428$ Mpc and to an angular to linear conversion scale of 4.233 $''$/kpc. Quoted errors are at 1σ confidence level for one parameter, unless otherwise stated.

2   THE DOUBLE CLUSTER ABELL 1758

Abell 1758 (hereafter A1758) is a galaxy cluster located at $z = 0.279$ that has been intensively studied in the literature. Early ROSAT data (Rizza et al. 1998) revealed that it consists of two components, A1758N (in the north) and A1758S (in the south), separated by a projected distance of ~ 8 arcmin (about 2 Mpc). David & Kempner (2004) estimated virial radii of 2.6 Mpc (for A1758N) and 2.2 Mpc (for A1758S), indicating that each cluster is affected by the potential well of the other and that they are gravitationally bound. Despite this, no signs of significant interaction between A1758N and A1758S were found by *Chandra* and *XMM-Newton* observations (David & Kempner 2004). However, from X-ray and optical studies, it is clear that the two sub-clusters are undergoing their own distinct mergers, with A1758N in a late and A1758S in an early merger state (e.g. David & Kempner 2004; Boschin et al. 2012). This might also be reflected in the infrared luminosity of the galaxies of A1758N, which is almost two times larger than that of A1758S, suggesting different dynamical histories for the two clusters (Haines et al. 2009). Weak lensing studies indicate that A1758N has a bimodal mass distribution, while A1758S represents a single mass clump (Dahle et al. 2002; Okabe & Umetsu 2008; Ragozzine et al. 2012; Monteiro-Oliveira et al. 2017). Individual mergers are possibly occurring near the plane of the sky for A1758N and close to the line of sight for A1758S.

So far, most studies have focused on A1758N which is more massive and hotter than A1758S (e.g. David & Kempner 2004). The mass of A1758N has been estimated using several methods (e.g. X-ray scaling relations, David & Kempner 2004; weak lensing, Okabe & Umetsu 2008; member galaxy dynamics, Boschin et al. 2012; hydrostatic equilibrium, Martino et al. 2014), providing a virial mass of $\sim 10^{15}$ M$_\odot$ which is split approximately equally between the two sub-components. This is further supported by hydrodynamical simulations, which can reproduce the X-ray morphology of A1758N assuming an off-axis collision of two equal mass ($\sim 5 \times 10^{14}$ M$_\odot$) clusters (Machado et al. 2015). A compilation of the different mass estimates reported for A1758N is given in Tab. 1 of Monteiro-Oliveira et al. (2017). Note that the mass of A1758S is more uncertain whilst it appears to be at least a factor of 1.5 smaller than that of A1758N (David & Kempner 2004; Ragozzine et al. 2012; Haines et al. 2017).

In the radio band, A1758N hosts a giant radio halo that was first detected by Kempner & Sarazin (2001) and later investigated at 1.4 GHz with the VLA (Giovannini et al. 2009, hereafter G09) and at 325 MHz with the GMRT (Venturi et al. 2013, hereafter V13). There are no reports of diffuse radio emission associated with A1758S in the literature.

3   OBSERVATIONS AND DATA REDUCTION

3.1   LOFAR

The LoTSS observations are typically separated by 2.6° and we have analyzed the LoTSS pointing that is centered closest to A1758 (offset by $\sim 1.1°$). The characteristics of this observation are summarized in Tab. 1. To calibrate the data we followed the facet calibration scheme described in van

Table 1. Summary of the radio observations used in this work.

	LOFAR	GMRT	VLA Array C	VLA Array D
Project code	LC2_038	11TVA01	AG639	
Pointing center (RA, DEC)	13h37m30s +49°44′53″	13h32m32s +50°30′37″	13h32m32s +50°30′36″	
Observation date	2014 Jun 1	2007 Mar 30/31	2004 May 6	2003 Mar 11
Total on-source time (hr)	8.0	8.0	2.5	2.5
Flux calibrator	3C196	3C147	3C286	
Total on-calibrator time (min)	10	26	10	9
Central frequency (MHz)	144	325	1425	
Bandwidth (MHz)	48	33	50	

Table 2. Imaging parameters for the radio images shown in the paper. The beam position angle (PA) is measured from north to east.

Fig.	Instrument	Frequency (MHz)	Robust	Taper (″)	Resolution (″ × ″)	PA (°)	rms (μJy beam^{-1})
1	LOFAR	144	+0.5	0	34 × 23	45	230
1	GMRT	325	0.0	35	43 × 29	29	400
1	VLA	1425	0.0	35	43 × 38	50	70
3	LOFAR	144	0.0	40	60 × 51	69	390
4	LOFAR	144	−0.5	10	16 × 11	88	140

Weeren et al. (2016b) and Williams et al. (2016). This procedure comprises three steps, which we describe below.

In the first step we perform direction-independent calibration (PREFACTOR[1] pipeline). In this step, the flux calibrator (3C196) data are averaged and bad quality data are flagged. Complex gains and clock offsets for different antenna stations are calibrated off a 3C196 model adopting the absolute flux density scale of Scaife & Heald (2012). The amplitude and clock solutions are then transferred to the target data before an initial phase calibration against a sky model generated from the TIFR GMRT Sky Survey-Alternative Data Release (TGSS-ADR1; Intema et al. 2017). In the second step, wide field images covering the full LOFAR field-of-view (FoV) are made from the products of the first step using WSClean (Offringa et al. 2014). The PYthon Blob Detector and Source Finder (PYBDSF; Mohan & Rafferty 2015) software is then used to detect sources which are then subtracted from the *uv*-data using the clean component models. Images are produced at medium ($\sim 40'' \times 30''$) and low resolution ($\sim 120'' \times 100''$) to ensure that both compact and extended sources are subtracted. The image sizes are about $12° \times 12°$ and $30° \times 30°$ for medium and low resolution, respectively.

In the direction-dependent calibration step (FACTOR[2] pipeline), nearly thermal noise limited images can be produced. It operates by using bright sources in the field to calibrate the phases and amplitudes in a restricted portion of the sky, i.e. a "facet". This is needed as the LOFAR primary beam is large, requiring many different corrections for ionospheric distortions and beam model errors across the FoV. For this reason, the FoV (usually a region within 2.5° from the pointing center) is divided into tens of facets that

are typically processed in order of decreasing flux density of the calibrator source. After a number of self-calibration cycles on the facet calibrator, the fainter sources that were subtracted in the second step are added back into the data and are calibrated using the solutions derived from the facet calibrator. An updated sky model of the region covered by the facet is obtained by subtracting the components of the processed facet from the *uv*-data. The *uv*-data that is then used for the calibration of the subsequent facet has smaller systematics due to the source subtraction and the effective noise in the dataset is reduced. This process is iteratively repeated until all the desired directions have been calibrated. This procedure has been successfully applied to image several other galaxy clusters with the LOFAR HBA (e.g. van Weeren et al. 2016a; de Gasperin et al. 2017; Hoang et al. 2017; Wilber et al. 2018).

All LOFAR images in the paper are reported at the central observing frequency of 144 MHz and were produced with CASA v4.7 (McMullin et al. 2007). The imaging was done using the multi-scale multi-frequency deconvolution algorithm (MS-MFS, Rau & Cornwell 2011), with second order Taylor terms (`nterms = 2`), and W-projection (Cornwell, Golap & Bhatnagar 2005). For the facet containing A1758, an image size of $5120'' \times 5120''$ was adopted to ensure that all of the sources in the vicinity of the cluster were adequately deconvolved. An inner *uv*-cut of 80λ (corresponding to an angular scale of $43'$) was also applied on the data to reduce sensitivity to very large scale emission from the Galaxy. Different resolution images were created using various different Briggs weightings (Briggs 1995) and by applying an *uv*-taper, as reported in Tab. 2. Primary beam correction was performed with AWimager (Tasse et al. 2013). Uncertainties in the flux scale that are caused by inaccuracies in the LOFAR HBA beam model (see van Weeren et al. 2016b; Hardcastle et al. 2016) were corrected by cross-matching a number of compact sources extracted from the LOFAR image with the

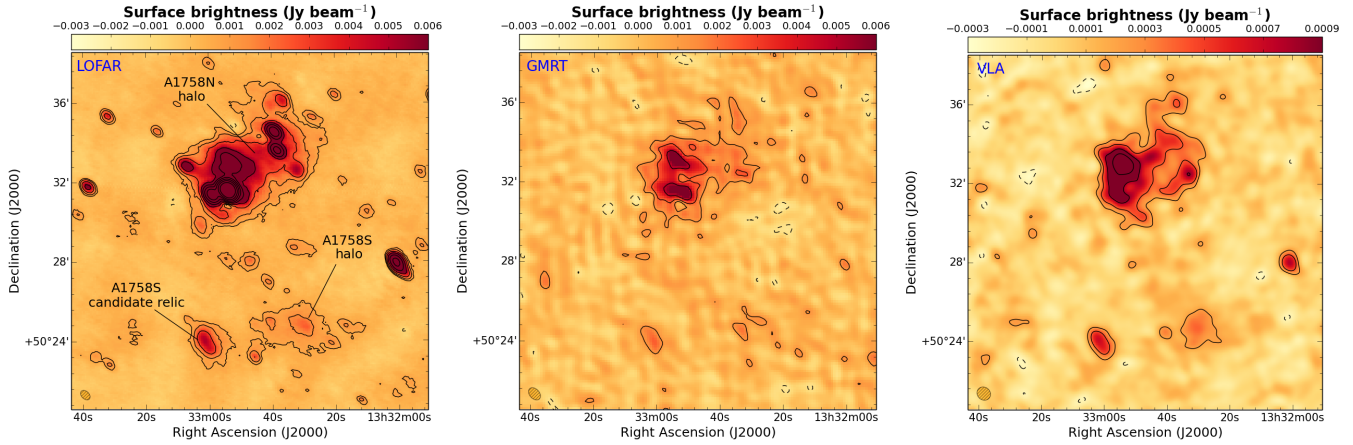[1] https://github.com/lofar-astron/prefactor
[2] https://github.com/lofar-astron/factor

Figure 1. The cluster A1758 as observed in the radio band with LOFAR (*left*), GMRT (*center*) and VLA (*right*). The point-sources were subtracted in the GMRT and VLA images. Contours are spaced by a factor of 2 starting from 3σ, where $\sigma_{\mathrm{LOFAR}} = 230~\mu$Jy beam^{-1}, $\sigma_{\mathrm{GMRT}} = 400~\mu$Jy beam^{-1} and $\sigma_{\mathrm{VLA}} = 70~\mu$Jy beam^{-1}. The negative -3σ contours are shown in dashed. The beam sizes are $34'' \times 23''$ (LOFAR), $43'' \times 29''$ (GMRT) and $43'' \times 38''$ (VLA) and are shown in the bottom left corners. More details on the images are reported in Tab. 2.

TGSS (Intema et al. 2017). Throughout the paper we have applied correction factor that was computed from the mean LOFAR/TGSS integrated flux density ratio of 1.08 and a calibration error of 15% on LOFAR flux densities, which is in agreement with other LOFAR HBA studies (e.g. Shimwell et al. 2016; Savini et al. 2018)

3.2   GMRT

We analyzed an 8 hr archival GMRT 325 MHz observation of A1758 (details in Tab. 1). Data were reduced with the Source Peeling and Atmospheric Modeling (SPAM) package (Intema et al. 2009), which is an automated pipeline to process GMRT observations based on the Astronomical Image Processing System (AIPS). Here we outline the main steps of the SPAM data reduction, for more details the reader is referred to Intema et al. (2009, 2017). First, the dataset is averaged in time and frequency to reduce the data processing time whilst keeping enough resolution in both time and frequency to avoid smearing. Bad data due to corrupted baselines, non-working antennas, and radio frequency interference were also excised. The bandpass and absolute flux density scale were calibrated using the primary flux calibrator 3C147 and adopting the Scaife & Heald (2012) flux scale. An initial phase-only calibration using a sky model generated from the VLA Low-frequency Sky Survey Redux (VLSSr; Lane et al. 2014), the WEsterbork Northern Sky Survey (WENSS; Rengelink et al. 1997) and the NRAO VLA Sky Survey (NVSS; Condon et al. 1998) was followed by a number of loops of self-calibration, wide-field imaging and additional flagging of bad data. Then the bright sources in the primary beam are used to perform a direction-dependent calibration and ionospheric modeling aiming to mitigate the phase errors introduced by the ionosphere. The final calibrated data were then imaged with CASA v4.7, in the manner that was described at the end of Section 3.1. In our analysis we did not consider the effect of variation in system temperature (see Sirothia 2009). Instead, we adopted a similar approach to that described in Section 3.1, cross-matching a

number of sources extracted from the GMRT image with the WENSS (Rengelink et al. 1997) and applying a correction factor of 0.73 on the GMRT flux densities with a systematic uncertainty of 15% (see Chandra, Ray & Bhatnagar 2004).

3.3   VLA

We analyzed archival VLA observations of A1758 at 1.4 GHz in configurations C and D. The details of the observations are reported in Tab. 1. Data reduction was performed with AIPS where the two datasets were edited, calibrated and imaged separately. Thus the *uv*-data were combined to produce a single image of the cluster. The flux calibrator of VLA observations was 3C286 (model from Perley & Butler 2013). The final imaging was performed with CASA v4.7 as described in Section 3.1. The absolute flux scale calibration errors were conservatively set to 5% on VLA flux densities.

3.4   Integrated synchrotron spectra and source subtraction

Given the different *uv*-coverage of the LOFAR, GMRT and VLA observations, it was necessary to match the *uv*-sample of the different interferometers as closely as possible to provide an accurate comparison between the flux densities measured at different frequencies, and to compute the diffuse emission spectra.

As a first step, we removed the discrete sources from each datasets. This procedure was performed by applying an inner *uv*-cut of 2.0 kλ (corresponding to an angular scale of $103''$, i.e. about 440 kpc at $z = 0.279$) to the data to image only the compact sources in the field whose clean components were subsequently subtracted from the visibilities. To image the diffuse emission after the source subtraction, for each dataset we used the an inner *uv*-cut of 170λ and `uniform` weighting. A Gaussian *uv*-taper of $35''$ was also used to enhance diffuse emission and to produce images with comparable beams. Errors on flux densities were estimated via

$$\Delta S = \sqrt{\left(\sigma_{rms} \times \sqrt{\frac{A_s}{A_b}}\right)^2 + (\xi \times S)^2} \qquad (1)$$

where ξ is the calibration uncertainty, σ_{rms} is the root-mean-square noise while A_s and A_b are the source and beam areas, respectively.

In Fig. 1 we present the LOFAR image (left panel) along with the point-source-subtracted images from the GMRT (central panel) and VLA (right panel). This choice has been made since the diffuse emission is best visible.

3.5 *Chandra*

We retrieved three ACIS-I observations (ObsID: 13997, 15538, 15540) on A1758 from the *Chandra* data archive[3] for a total exposure time of 150 ks. We mention that two other *Chandra* pointings on A1758 also exist; however they composed of an ACIS-S observation where only A1758N is in the FoV (ObsID 2213) and by a short (7 ks) observation (ObsID 7710) whose exposure time is negligible with respect to the total integration time. For that reason they were not used in this work.

Data reduction was performed with CIAO v4.9 and *Chandra* CALDB v4.7.3. Time periods affected by soft proton flares were removed by inspecting the light curves in the $0.5 - 7.0$ keV band extracted for each ObsID from the S2 chip with the `lc_clean` routine. After this step, the resulting clean exposure time is 137 ks. We used `merge_obs` to add together the three datasets and produce the final cluster image in the $0.5 - 2.0$ keV band. An exposure-corrected point spread function (PSF) map with minimum size was created from the combination of the PSF and exposure maps of the three ObsIDs. This was used to detect discrete sources with the `wavdetect` task, which were later confirmed by eye and excluded in the further analysis.

Spectra were extracted in the same regions from all the ObsIDs and simultaneously fitted in the $0.5 - 10.0$ keV band with XSPEC v12.9.0o (Arnaud 1996). The background was carefully treated with a model that included both astrophysical and instrumental emission components, as shown in Fig. 3. The former is described by two main components due to: the Galactic emission, modeled with two thermal plasmas with $kT_1 = 0.14$ keV and $kT_2 = 0.25$ keV, and the cosmic X-ray background, described with an absorbed power-law with photon index $\Gamma = 1.4$. For the latter we followed Bartalucci et al. (2014) which provided an analytical model for the ACIS-I particle background. Spectra were fitted adopting Cash statistics (Cash 1979) and an absorbed thermal model for the ICM with metallicity fixed at 0.3 $Z_\odot$ (solar abundance table by Anders & Grevesse 1989) and hydrogen column density $N_H = 1.03 \times 10^{20}$ cm^{-2} computed from the Leiden/Argentine/Bonn Survey of Galactic H I (Kalberla et al. 2005).

We used CONTBIN v1.4 (Sanders 2006) to compute the thermodynamical properties of the ICM in A1758. A signal-to-noise ratio (S/N) of 50 for the net counts in the $0.5 - 2.0$ keV band was set to delineate the regions where spectra were extracted and fitted as written above. For more details on the computation of the maps of the ICM thermodynamical
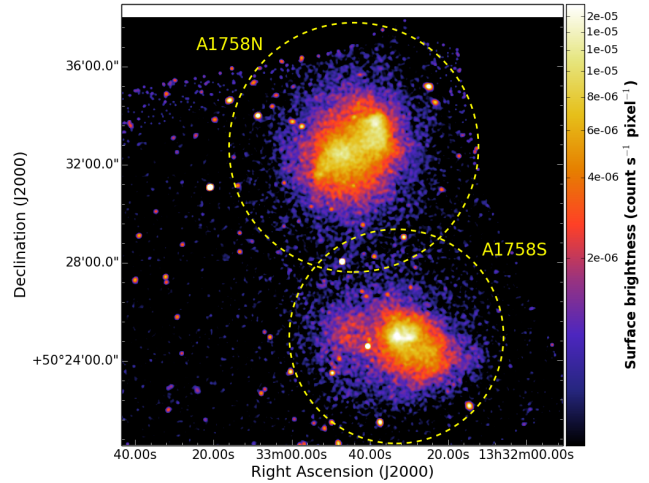
[3] http://cda.harvard.edu/chaser/

Figure 2. *Chandra* exposure-corrected image in the $0.5-2.0$ keV band of A1758 smoothed to a resolution of $\sim 3''$. Yellow circles indicate the approximate location of r_{500} for each cluster.
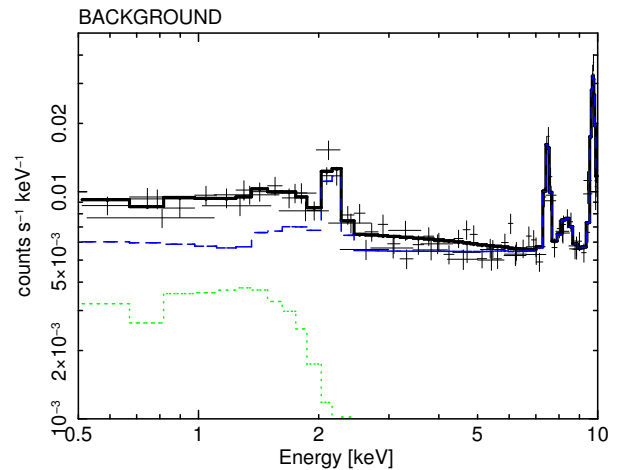

Figure 3. Spectrum of the *Chandra* background. Data points are shown in black together with the best-fitting model. The astrophysical and instrumental backgrounds are shown in dotted green and dashed blue, respectively. Whilst the three ObsID spectra were simultaneously fitted, the models for only one observation were reported in order to avoid confusion in the plot. The c-stat/d.o.f. of the fit is 406/386.

quantities and generally on the *Chandra* data analysis we refer the reader to Botteon, Gastaldello & Brunetti (2018) in which the same procedures adopted in the current paper have been more thoroughly described.

4 RESULTS

4.1 A1758N radio halo

Diffuse emission in A1758N is visible both from the NVSS and the WENSS surveys (Kempner & Sarazin 2001). The observations taken with the VLA at 1.4 GHz (G09) and with the GMRT at 325 MHz (V13) confirmed the presence of a giant radio halo which is elongated in the NW-SE direction and only partially covering the X-ray emission of the
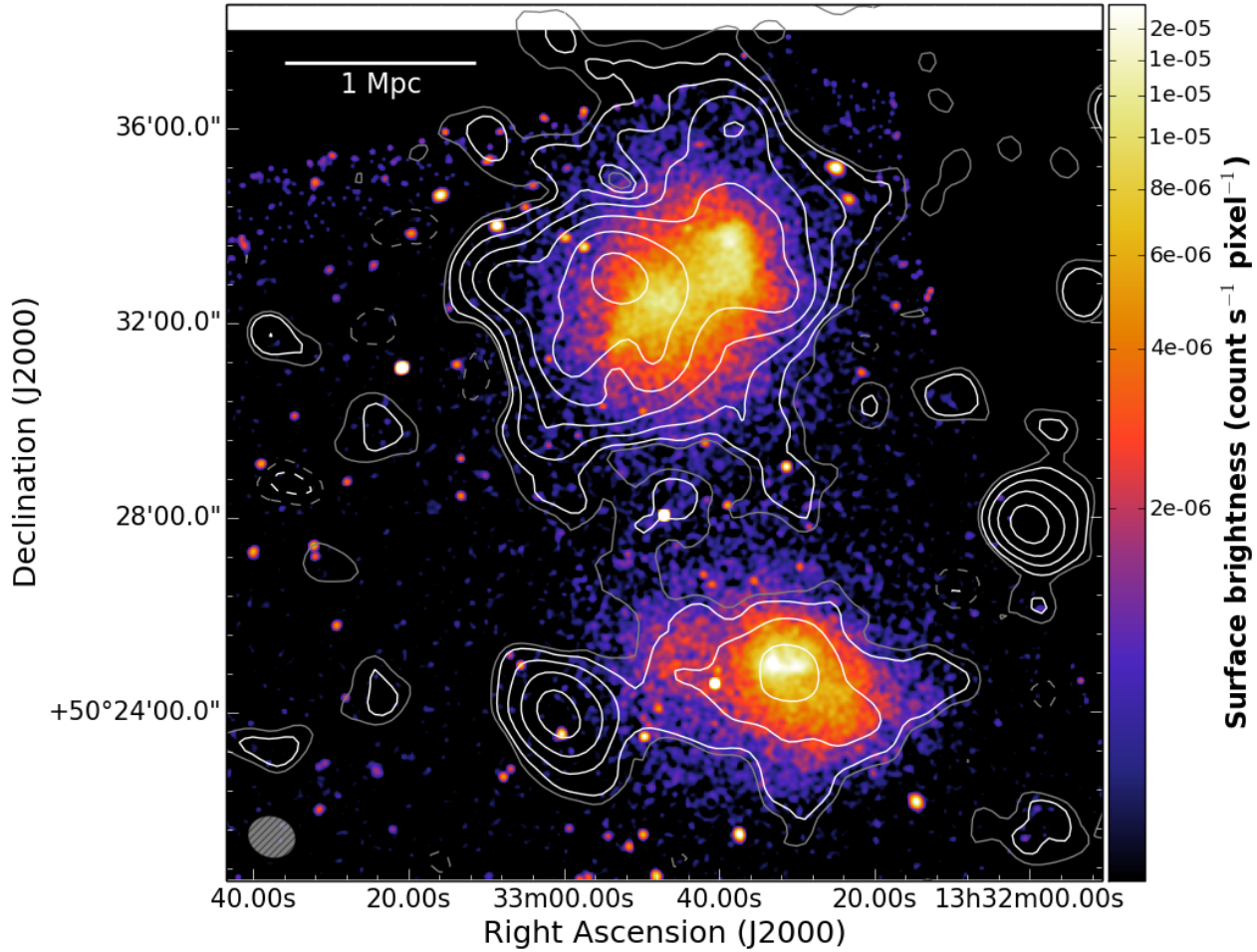
Figure 4. LOFAR radio contours with point-sources subtracted of A1758 overlaid on the *Chandra* color image of Fig. 2. The LOFAR white contours are spaced by a factor of 2 starting from 3σ, where $\sigma_{\mathrm{LOFAR}} = 390$ μJy beam^{-1}. The negative -3σ contours are shown in dashed. Gray contours correspond to the $\pm 2\sigma$ level. The beam size is $60'' \times 51''$ and is shown in the bottom left corner. More details on the LOFAR image are reported in Tab. 2.
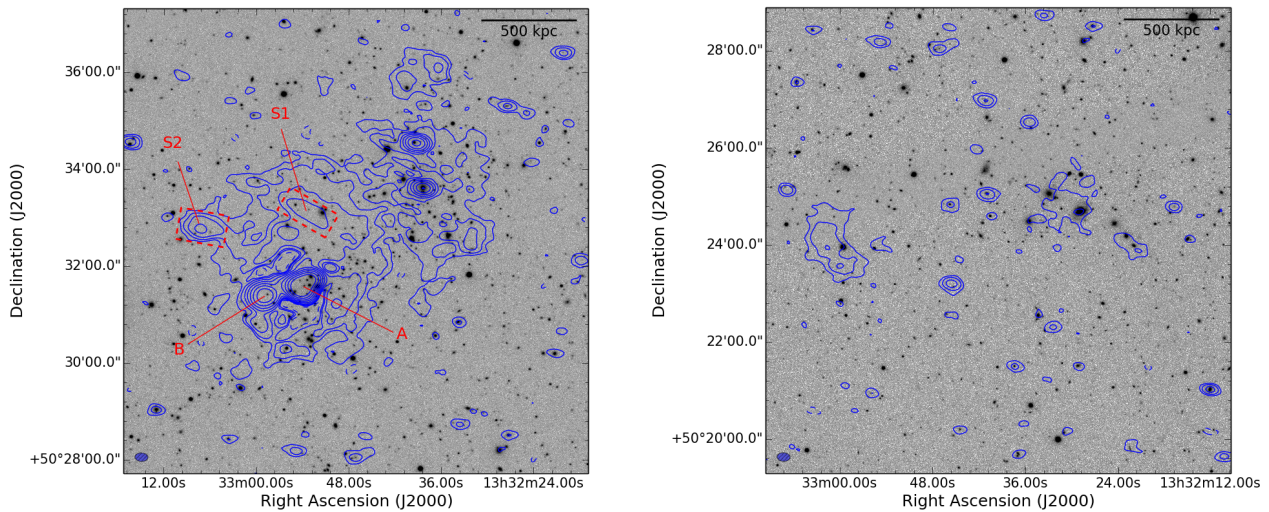

Figure 5. Mosaic SDSSg,r,i images of A1758N (*left*) and A1758S (*right*) overlaid with the LOFAR contours spaced by a factor of 2 starting from 3σ, where $\sigma_{\mathrm{LOFAR}} = 140$ μJy beam^{-1}. The negative -3σ contours are shown in dashed. The beam size is $16'' \times 11''$ and is shown in the bottom left corners. At this resolution the radio halo in A1758S is marginally visible. More details on the LOFAR image are reported in Tab. 2.
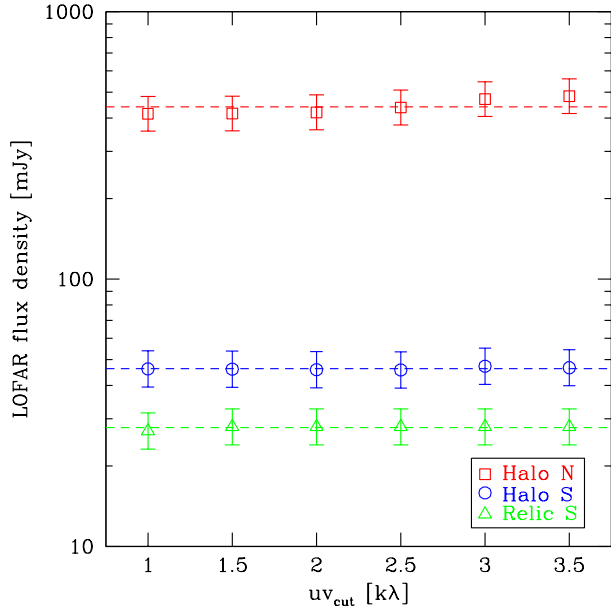
Figure 6. The flux densities of the diffuse emission in A1758 measured with LOFAR versus the inner uv-cuts adopted to subtract the point-sources. Dashed horizontal lines show the mean values of the measurements.
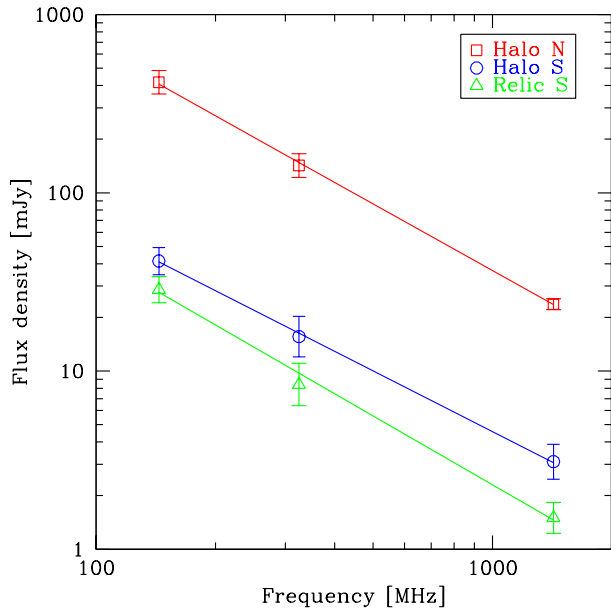

Figure 7. Integrated spectra of the diffuse radio emissions in A1758. The spectral index values are reported in Tab. 3.

Table 3. Flux densities of the diffuse emission in A1758. The spectral indexes were computed adopting the procedure described in Section 3.4.

ν [MHz]		S_ν [mJy]	
	Halo N	Halo S	Relic S
144	420 ± 63	45.8 ± 7.1	28.0 ± 4.3
325	134 ± 20	16.8 ± 3.5	8.9 ± 2.0
1425	$24.7 \pm 1.7^\dagger$	$3.1 \pm 0.7^\dagger$	1.5 ± 0.3
α	1.2 ± 0.1	1.1 ± 0.1	1.3 ± 0.1

Notes. † The error takes into account also the uncertainties of the source subtraction.

thermal radio emission in A1758N covers the X-ray bright region of the cluster. At higher resolution (Fig. 5, left panel), only the brightest part of the radio halo is visible; in particular, LOFAR shows two bright and straight structures (labeled as S1 and S2 in Fig. 5, left panel) apparently not associated with any optical galaxy. They might indicate regions where the plasma has been somehow locally compressed or re-accelerated (e.g. Shimwell et al. 2016; de Gasperin et al. 2017). The feature S1 is also detected with the GMRT and VLA (Fig. 1). In the southeast, A1758N also hosts two prominent narrow angle tailed radio galaxies labeled as A and B in Fig. 5 (left panel). The former (also identified as $1330 + 507$) was studied at high resolution with the VLA by O'Dea & Owen (1985).

The presence of resolved radio galaxies embedded in the halo (e.g. source A and B in Fig. 5, left panel) makes it difficult to disentangle their contribution from that of the halo. We repeated the subtraction by adopting inner uv-cuts in the range $1.0 - 3.5$ kλ, corresponding to linear sizes of $873 - 249$ kpc at the cluster redshift, to assess the uncertainties in our source subtraction on the LOFAR dataset, in addition to the procedure described in Section 3.4. In Fig. 6 we show how the flux density measurement of the northern radio halo varies with the uv-cut, ranging from 415 to 483 mJy (the mean value is 440 mJy). This indicates that the choice of the uv-cut has an impact on the halo in A1758N. In contrast, the integrated flux density of the diffuse sources in A1758S (see Sections below) is essentially independent on the uv-cut used (Fig. 6), indicating that the subtraction is less problematic which is expected as there are just a few weak discrete sources without significant extended emission (cf. Fig. 5, right panel).

In Tab. 3 and Fig. 7 we report the flux density measurements at three frequencies and the spectra, respectively, of the diffuse emission in A1758. The spectral index between 144 MHz and 1.4 GHz is $\alpha = 1.2\pm0.1$ for the halo in A1758N, consistent with that of $\alpha = 1.31 \pm 0.16$ computed by V13. The flux densities measured in our GMRT and VLA images agree to that reported in V13 within 1σ. The emission from the potential relic and the halo in A1758S have not been previously reported.

4.2 A1758S radio halo

The halo in A1758S is barely visible with the GMRT and it is detected at low significance with the VLA (Fig. 1). The characteristics of the emission recovered by the LOFAR ob-
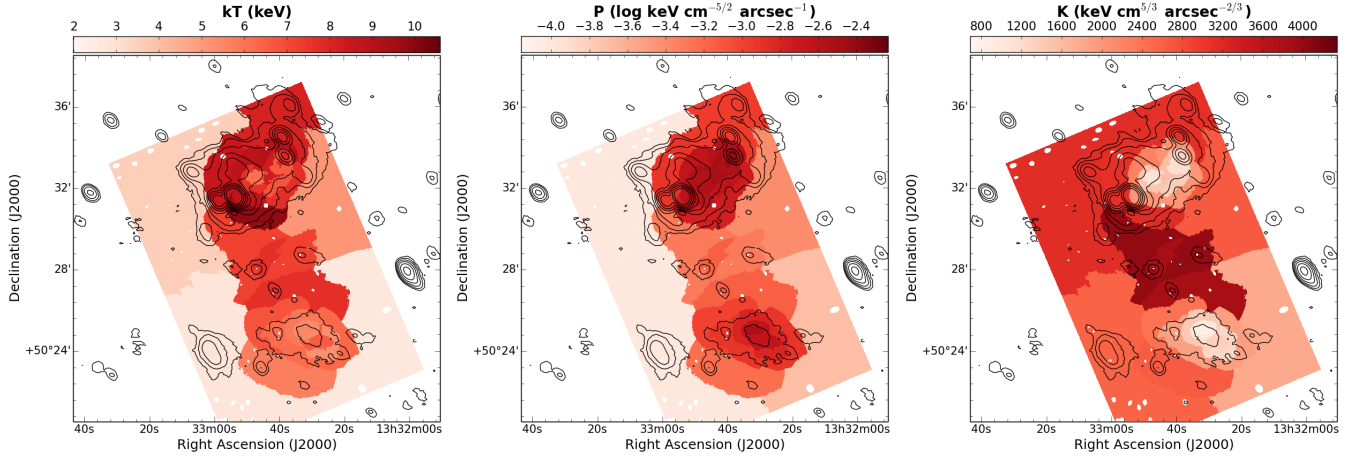
cluster. The spectral index reported between these two frequencies is $\alpha = 1.31 \pm 0.16$ (V13).

LOFAR detects the extended radio halo flux in A1758N at higher significance and the recovered morphology appears consistent with the GMRT and VLA maps, as demonstrated in Fig. 1. We measure a largest linear size of the emission of ~ 2.2 Mpc. The low resolution point-source-subtracted LOFAR contours displayed in Fig. 4 suggest that the non-

Figure 8. Thermodynamical properties of the ICM in A1758 with overlaid the LOFAR contours of Fig. 1. Images depict projected values of temperature (*left*), pressure (*center*) and entropy (*right*). The temperature error map and a lower S/N temperature map are reported in Appendix A.

servation (Fig. 4) are typical for a radio halo, i.e. low surface brightness, similar morphology with respect to the ICM thermal emission and a largest linear size of ~ 1.6 Mpc. It is worth noting that the merger axis of A1758S is likely close to the line of sight (e.g. Monteiro-Oliveira et al. 2017), hence we can not fully discard the possibility that the radio emission traces a radio relic observed face-on, although this is unlikely because the remarkable similarity between the radio and the X-ray emission (Fig. 4). Future studies on the source polarization level will definitely clarify this point.

The integrated flux density measured with LOFAR within the 3σ contour from the low resolution image of Fig. 4 (excluding the peripheral emission to the east, see Section below) is 45.8 ± 7.1 mJy, i.e. one order of magnitude lower than that of the halo in A1758N. Indication of the presence of a radio halo in A1758S has also been found in the Westerbork Synthesis Radio Telescope (WSRT) data at 367 MHz (Drabent 2017). However, the available observation is not suitable to study in detail the diffuse emission due to its inadequate angular resolution which makes the point-source subtraction unreliable. The spectral index computed between 144 MHz and 1.4 GHz within a region traced by the LOFAR emission is $\alpha = 1.1 \pm 0.1$ (see Tab. 3) and the fit is shown in Fig. 7. We also determined the halo spectral index considering a region defined by the VLA 3σ contour. In this case, the flux densities evaluated in the LOFAR and VLA images are ~ 12.5 mJy and ~ 1.2 mJy, respectively, and the spectral index is consistent with that reported above.

4.3   A1758S candidate radio relic

To the east of A1758S, an extended radio source at the boundaries of the X-ray emission is observed with LOFAR, GMRT and VLA (Fig. 1). In the LOFAR low resolution contours of Fig. 4, the 3σ contour of this emission is connected with that of the radio halo. In Tab. 3 we report the flux density measurements at various frequencies. We estimated a spectral index between 144 MHz and 1.4 GHz of $\alpha = 1.3 \pm 0.1$ for this source (Fig. 7). We tentatively classify this emission as a radio relic based on the following characteristics: (i) its elongated morphology roughly arc-shaped

and perpendicular to the thermal cluster emission, (ii) its largest linear size > 500 kpc, (iii) its peripheral location in the same direction of the ICM elongation, (iv) its steep spectrum, and (v) the absence of a clear optical counterpart[4] and/or bright compact radio emission (Fig. 5, right panel). All these properties are commonly observed in radio relics but can also be seen in other objects, such as dead radio galaxies (e.g. Brienza et al. 2016, and references therein). A definitive claim would require either the study of the spectral index gradient toward the cluster center, measurements of the source polarization or the detection in the X-rays of an underlying shock front. Unfortunately none of these measurements can be carried out with the present data.

4.4   X-ray properties of A1758N and A1758S

The deep *Chandra* observation of A1758 allowed us to derive the projected maps of the ICM thermodynamical quantities shown in Fig. 8. The temperature map displays overall higher values in A1758N than in A1758S. These values are within the range of $8.0 - 9.9$ keV, for A1758N, and $6.0 - 6.7$ keV, for A1758S, that were reported by David & Kempner (2004) who made measurements within 1 Mpc radius aperture centered on the centroid of each cluster. Shock heated regions toward the NW and SE of the northern cluster are suggested by high values of temperature and pressure (Fig. 8, see also Fig. A2), in agreement with the late merger scenario (David & Kempner 2004) where the shocks have already crossed the central region of the ICM and are moving outwards with high Mach numbers (Machado et al. 2015). Our entropy map of Fig. 8 (right panel) highlights the presence of the two cores in A1758N and the single core

---

[4] Note that the source roughly at the center of the diffuse radio emission in the optical image of Fig. 5 (right panel) is a star. No redshift has been reported for the X-ray point source (identified as SDSS J133300.32+502332.2) embedded in the candidate relic that is visible in the *Chandra* image of Fig. 4. With the current data we can not conclude whether it is associated with the radio emission.
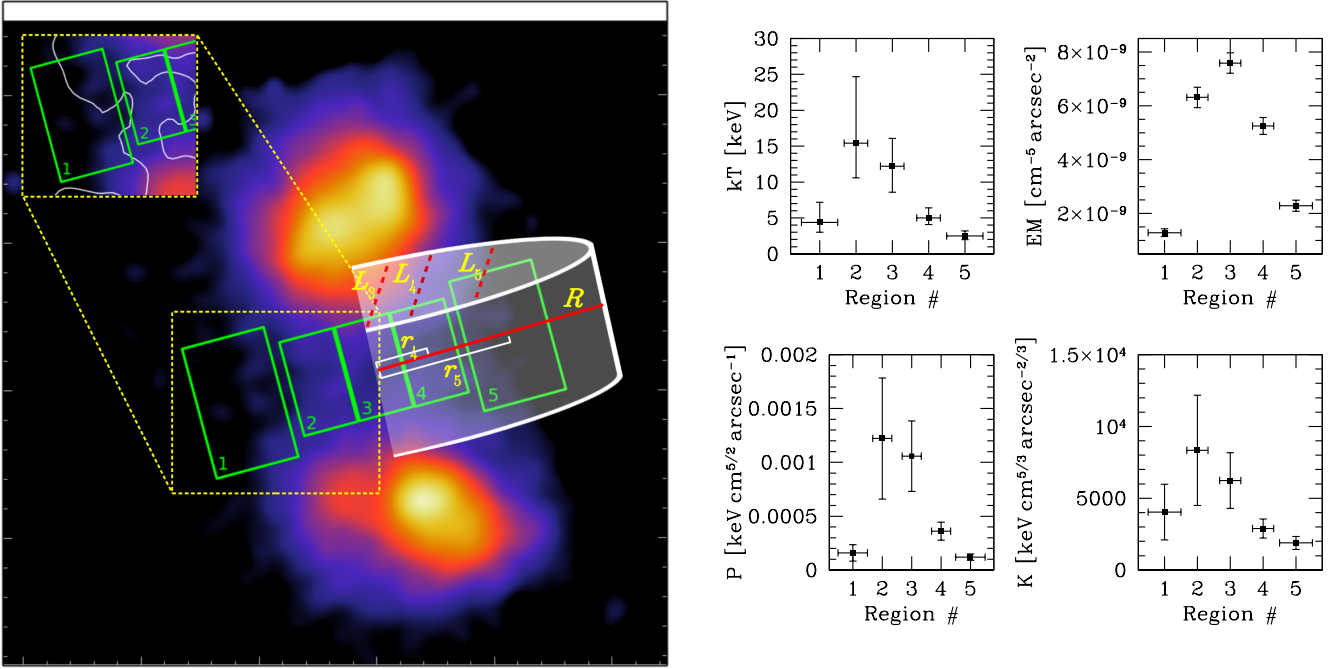
Figure 9. *Left panel*: same *Chandra* image of Fig. 2 but with point-sources subtracted and smoothed to a resolution of $\sim 15''$ to highlight the X-ray channel between the clusters. The spectral extracting regions are overlaid in green. The inset panel shows the spatial coincidence between the tentative radio bridge and the putative post-shock region. The cylindrical model assumed to asses the effects of projection is also sketched. The line of sight across the i-region is $L_i \sim 2\sqrt{R^2 - r_i^2}$. *Right panels*: projected values of temperature (kT), emission measure (EM), pressure (P) and entropy (K) of the X-ray channel.

4.5 The bridge between A1758N and A1758S

The maps of the ICM thermodynamical quantities shown in Fig. 8 show a complex thermodynamics in the region between A1758N and A1758S, suggesting that the two clusters are in early interaction. At this stage of the interaction the gas between them is compressed and heated, somewhat explaining the observed high values of temperature (~ 7.5 keV) and pressure in the region between the cluster pair. Moreover, the entropy map (Fig. 8, right panel) displays the largest values in such a region, further indicating an unrelaxed state of the clusters outskirts.

The LOFAR low resolution contours of Fig. 4 give a tantalizing hint of a low surface brightness bridge connecting A1758N and A1758S. This emission is detected at the 2σ level towards the eastern edge of the region between the two clusters. On the western edge of this region, a protuberance of the A1758N halo extends towards A1758S. Although particular care was devoted in the subtraction of the point-sources between the clusters, the blending of low level residual emission due to faint and unresolved sources, combined with the large synthesized beam of the image and with the non-uniform distribution of the noise, could mimic the filamentary structure. All this, together with the low significance level of the emission, does not allow us to make

a firm statement about its presence. Nonetheless, filaments connecting galaxy clusters are expected to be observed in the radio band even on larger scales (e.g. Keshet, Waxman & Loeb 2004; Araya-Melo et al. 2012; Vazza et al. 2015b). We note that a hint of a Sunyaev-Zel'dovich (SZ) signal connecting A1758N and A1758S was reported also in AMI Consortium: Rodrìguez-Gonzálvez et al. (2012).

We analyzed the thermal properties of the X-ray emission between A1758N and A1758S, visible by smoothing to a resolution of $\sim 15''$ the *Chandra* $0.5-2.0$ keV image (Fig. 9, left panel). We extracted spectra from five regions enclosing ~ 1000 counts each in the $0.5-2.0$ keV band that were fitted as described in Section 3.5. The best-fitting spectra are reported in Appendix B. These were used to compute the temperature profile shown in Fig. 9 (right panel). We measure high kT values inside the X-ray channel that drop by a factor of ~ 3 between regions 2 and 1 (see Appendix A for the apparent discrepancy between the values of the temperature map and profile shown in Fig. 9); if projection effects play a role, the temperature drop would be even larger. Unfortunately, the count statistics does not allow us to increase spatial resolution to firmly understand if this is sharp drop or a gradual decrement. If we assume that this is a jump due to a shock and we apply the Rankine-Hugoniot jump conditions (e.g. Landau & Lifshitz 1959)

$$\frac{T_2}{T_1} = \frac{5\mathcal{M}_{kT}^4 + 14\mathcal{M}_{kT}^2 - 3}{16\mathcal{M}_{kT}^2} \tag{2}$$

the derived Mach number[5] would be $\mathcal{M}_{kT} = 3.0^{+1.4}_{-1.0}$. We

---

[5] Although also the surface brightness drops outside the X-ray

notice that this putative shock is co-located with the 2σ level emission observed by LOFAR (Fig. 9, inset in the left panel). This is tantalizing and deserves future follow-ups as it might suggest a connection between the shock and the possible radio bridge. Its uncommonly high Mach number and unusual transversal location are in agreement with the recent work of Ha, Ryu & Kang (2018), where these kind of shocks are referred as "equatorial". Alternatively, the high kT values of the X-ray channel could be due to the adiabatic compression of the gas in the filament connecting A1758N and A1758S during the initial stage of the merger.

As a complementary information, the five spectra were used to compute the profiles of emission measure, pressure and entropy shown in Fig. 9 (right panel). These quantities are also observed to jump from the external to internal regions. We urge caution when interpreting these measurements as they were derived from the normalization of the cluster thermal model, that is $\propto n^2 L$, and are projected along the line of sight L (n is the density of the medium). For this reason they are usually referred as "pseudo" quantities (e.g. Mazzotta et al. 2004). We can asses the effects of projection assuming a cylindrical shape for the X-ray channel (Fig. 9, left panel) and using the dependencies on the line of sight of the emission measure ($\propto L^{-1}$), pressure ($\propto L^{-1/2}$) and entropy ($\propto L^{1/3}$). For example, the ratio between the quantities measured at center and r_5 ($\equiv r_1$), i.e. the distance of the outermost region, changes by $< 16\%$ (or $< 34\%$) for emission measure, $< 8\%$ (or $< 16\%$) for pressure and $< 4\%$ (or $< 10\%$) for entropy for cylinder radii $R > 2r_5$ (or $> 1.5r_5$).

5   DISCUSSION

A1758 is an ideal object to study the merger processes between galaxy clusters and the impact of these events on their environment. Indeed, this system is composed of two main components, A1758N and A1758S, in different evolutionary stages (see Section 2).

The diffuse radio emission in A1758 follows the X-ray emission of the ICM (Fig. 4), suggesting a relation between the thermal and non-thermal components. The double cluster A1758N and A1758S represents the second system known to date to host two radio halos. The first discovered is the pair A399-A401 (Murgia et al. 2010), located at $z = 0.07$. Both A1758 and A399-A401 show the presence of an X-ray channel between the cluster pair and some evidence for a lateral shock (Akamatsu et al. 2017). The bridge connecting A399 and A401 is more clear and indeed it has been also observed via the SZ effect by the *Planck* satellite (Planck Collaboration VIII 2013); a hint of SZ signal is also found between A1758N and A1758S (AMI Consortium: Rodrìguez-Gonzálvez et al. 2012).
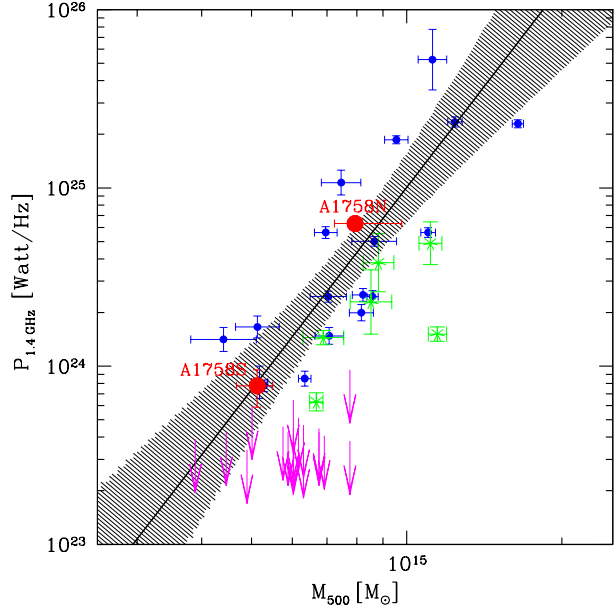

Figure 10. The $P_{1.4} - M_{500}$ relation for giant radio halos. Different colors indicate: giant radio halos (*blue*), ultra steep spectrum radio halos (*green*), upper limits from Venturi et al. (2008) (*magenta*) and the radio halos in A1758N and A1758S (*red*). Errors on $P_{1.4}^{\rm N}$ are smaller than the point size. The best-fitting relation for giant radio halos and its 95% confidence level are shown. Adapted from Cassano et al. (2013).

5.1   The radio halos in the A1758 complex

It is known that giant radio halos follow a relation between their radio power at 1.4 GHz and the mass of the hosting cluster (e.g. Cassano et al. 2013). We used the values reported in Tab. 3 to calculate the k-corrected 1.4 GHz radio power

$$P_{1.4} = 4\pi S_{1.4} D_L^2 (1+z)^{\alpha - 1} \tag{3}$$

for the two halos in A1758N and A1758S, corresponding to $P_{1.4}^{\rm N} = (6.3 \pm 0.4) \times 10^{24}$ W Hz^{-1} and $P_{1.4}^{\rm S} = (7.7 \pm 1.8) \times 10^{23}$ W Hz^{-1}, respectively.

The $P_{1.4} - M_{500}$ relation reported in Cassano et al. (2013) was obtained using the masses derived from the *Planck* satellite via SZ effect, which is known to be a robust indicator of the cluster mass (e.g. Motl et al. 2005; Nagai 2006). However, the accuracy of the mass estimate for A1758N and A1758S with *Planck* is hindered by the difficulty of properly separating the two SZ components. Although the mass for A1758N has been estimated with different techniques, it is still uncertain and there is a large scatter in the values reported in the literature (see Tab. 1 in Monteiro-Oliveira et al. 2017). The mass of A1758S is even more uncertain due to the lack of literature studies focused on this sub-cluster. In this respect, we adopted the $M-T$ relation reported in Arnaud, Pointecouteau & Pratt (2005) to

channel, we did not attempt the "canonical" broken power-law density profile fit (e.g. Markevitch & Vikhlinin 2007) to search for the edge due to the complex geometrical problem at this location (overlap of the outskirts of two galaxy clusters).

estimate M_{500}. We used the temperatures reported in David & Kempner (2004), and derived $M_{500}^{N} = 8.0^{+1.8}_{-0.8} \times 10^{14}$ $M_{\odot}$ and $M_{500}^{S} = (5.1 \pm 0.4) \times 10^{14}$ $M_{\odot}$ for A1758N and A1758S, respectively. We assumed these values being aware of the possible biases introduced in the scaling relation due to the ongoing mergers in A1758N and A1758S. However, we note that the masses estimated in such a way are within the values reported in the literature.

In Fig. 10 we compare our results with the $P_{1.4} - M_{500}$ relation reported in Cassano et al. (2013). The two radio halos in the A1758 complex lie very close to the best-fitting curve. Our results are in agreement with the fact that the most powerful radio halos are found in the most massive clusters.

5.2 Merger scenario between A1758N and A1758S

David & Kempner (2004) did not find any excess emission in the *XMM-Newton* data in the region between A1758N and A1758S above that expected from a projection of the two systems. This suggested that the two components are not interacting because numerical simulations of merging clusters predict a surface brightness enhancement in the X-rays in the region of interaction (e.g. Roettiger, Loken & Burns 1997; Ricker & Sarazin 2001; Ritchie & Thomas 2002). However, our observations provide new insights on the merger scenario between A1758N and A1758S.

Thanks to the new and deep *Chandra* observations we were able to produce maps of the ICM thermodynamical quantities of all the A1758 complex (Fig. 8). They highlight the presence of high temperature and high entropy plasma in the region between the clusters, suggesting the existence of shock heated gas. This has been observed in a number of binary X-ray clusters in an early merging phase (e.g. A98, Paterno-Mahler et al. 2014; A115, Gutierrez & Krawczynski 2005; A141, Caglar 2018; A399-A401, Akamatsu et al. 2017; A1750, Belsole et al. 2004; A3395, Lakhchaura et al. 2011; A3653, Caglar & Hudaverdi 2017; 1E2216.0-0401 and 1E2215.7-0404, Akamatsu et al. 2016; CIZA J1358.9-4750, Kato et al. 2015) and it is in agreement with predictions by numerical simulations (e.g. Takizawa 1999; Akahori & Yoshikawa 2010). In contrast, the temperature enhancement is typically not observed when the separation of the pair exceeds their combined virial radii (e.g. A2467 Wegner et al. 2017; A3528, Gastaldello et al. 2003; A3556-A3558, Mitsuishi et al. 2012; A3716, Andrade-Santos et al. 2015). Further indication of compressed gas in A1758 is given by the transversal profiles of Fig. 9 that also pinpoint a drop of the computed quantities outside the X-ray channel, toward the east direction. We speculated that this region traces a transversal shock. Reasons for this include the high Mach number inferred from the temperature jump ($\mathcal{M}_{kT} = 3.0^{+1.4}_{-1.0}$) and its position resembling that of the "equatorial" shocks recently studied by Ha, Ryu & Kang (2018). These shocks are the first to form during the merger phase and have high velocities and high Mach numbers since they propagate in very low density regions, contrary to those found in between the cluster pairs that are weaker due to the high temperature of the central medium (e.g. Belsole et al. 2004; Paterno-Mahler et al. 2014; Kato et al. 2015; Akamatsu et al. 2016, 2017; Caglar 2018).

The 2σ level radio emission connecting A1758N and A1758S observed with LOFAR (Fig. 4) needs further confirmation. If real, it could have been generated as a consequence of the encounter between the two clusters. This may indicate that part of the gravitational energy is dissipated into non-thermal components during the early phase of the merger. We find intriguing its co-location with the possible transversal shock suggested by the temperature profile in Fig. 9 (see also Fig. A2). A shock could indeed power the radio emission similarly to the case of radio relics, whilst equatorial shocks are less energetic due to the lower density of the upstream gas[6] (Ha, Ryu & Kang 2018).

In conclusion, the results coming from our radio/X-ray analysis are consistent with a scenario where A1758N and A1758S are in a pre-merger phase, where the clusters are approaching, the gas between them is compressed and heated and the first shocks are launched. The application of a two-body dynamical model (e.g. Beers, Geller & Huchra 1982) to test the gravitational binding of the clusters would be of great interest to probe the merging scenario; however, this is beyond the scope of this paper. Due to the overall complex dynamics of the merger (collision between clusters that are undergoing their own mergers), tailored numerical simulations would be useful to determine the impact velocities of the components in combination with multi-wavelength data (see e.g. Molnar et al. 2013 for the A1750 case).

6 CONCLUSIONS

We have presented new LOFAR HBA observations of the double galaxy cluster A1758. In combination with archival VLA and GMRT data, we have constrained the spectral properties of the diffuse radio emission in the ICM. We also analyzed a deep archival *Chandra* observation on the system. Here, we summarize our main results.

(i) The radio halo in A1758N is well known in the literature. LOFAR has allowed us to recover diffuse radio emission from the ICM on a largest linear scale of ~ 2.2 Mpc. The integrated spectral index computed from 144 MHz to 1.4 GHz is $\alpha = 1.2 \pm 0.1$. The radio power of this halo is $P_{1.4}^{N} = (6.3 \pm 0.4) \times 10^{24}$ W Hz^{-1}.

(ii) Using LOFAR we have discovered a new, faint, radio halo in A1758S, which was not previously identified in studies at higher frequencies with the GMRT and VLA observations. Our reanalysis of these datasets revealed its elusive nature and constrained its spectral index between 144 MHz and 1.4 GHz to $\alpha = 1.1 \pm 0.1$. The radio power of this halo is $P_{1.4}^{S} = (7.7 \pm 1.8) \times 10^{23}$ W Hz^{-1}.

(iii) Peripheral emission in the eastern outskirts of A1758S is also observed with LOFAR, GMRT and VLA. We tentatively classified this source as a radio relic ($\alpha = 1.3 \pm 0.1$). Although the relic origin is suggested by a number of observational properties (e.g. morphology, location, linear extension), further observations are required

---

[6] The energy dissipated by shocks is $\propto n_u V_{sh}^3$, where n_u is the upstream density and V_{sh} is the shock speed.

to firmly determine its nature.

(iv) The two radio halos in A1758N and A1758S lie within the 95% confidence region of the best-fitting $P_{1.4} - M_{500}$ relation reported by Cassano et al. (2013).

(v) The maps of the ICM thermodynamical quantities computed from the deep *Chandra* observation indicate that the region between A1758N and A1758S is unrelaxed. In this respect, we suggested that the two sub-clusters are in a pre-merger phase.

(vi) A possible bridge of radio emission connecting A1758N and A1758S is suggested by the low resolution LO-FAR image. The ICM temperature across this bridge shows a drop possibly indicating the presence of a compressed region or a transversal shock generated in the initial stage of the merger that could play a role in the formation of this diffuse emission.

REFERENCES

Akahori T., Yoshikawa K., 2010, PASJ, 62, 335
Akamatsu H. et al., 2017, A&A, 606, A1
Akamatsu H. et al., 2016, A&A, 593, L7
Akamatsu H., Kawahara H., 2013, PASJ, 65, 16
AMI Consortium: Rodrìguez-Gonzálvez C. et al., 2012, MNRAS, 425, 162
Anders E., Grevesse N., 1989, Geochim. Cosmochim. Acta, 53, 197
Andrade-Santos F. et al., 2015, ApJ, 803, 108
Araya-Melo P., Aragón-Calvo M., Brüggen M., Hoeft M., 2012, MNRAS, 423, 2325
Arnaud K., 1996, in Astronomical Society of the Pacific Conference Series, Vol. 101, Astron. Data Anal. Softw. Syst. V, Jacoby G., Barnes J., eds., p. 17
Arnaud M., Pointecouteau E., Pratt G., 2005, A&A, 441, 893
Bartalucci I., Mazzotta P., Bourdin H., Vikhlinin A., 2014, A&A, 566, A25
Beers T., Geller M., Huchra J., 1982, ApJ, 257, 23
Belsole E., Pratt G., Sauvageot J.-L., Bourdin H., 2004, A&A, 415, 821
Bonafede A., Intema H., Brüggen M., Girardi M., Nonino M., Kantharia N., van Weeren R., Röttgering H., 2014, ApJ, 785, 1
Boschin W., Girardi M., Barrena R., Nonino M., 2012, A&A, 540, A43
Botteon A., Gastaldello F., Brunetti G., 2018, MNRAS, 476, 5591
Botteon A., Gastaldello F., Brunetti G., Dallacasa D., 2016a, MNRAS, 460, L84
Botteon A., Gastaldello F., Brunetti G., Kale R., 2016b, MNRAS, 463, 1534
Brienza M. et al., 2016, A&A, 585, A29
Briggs D., 1995, in Bulletin of the American Astronomical Society, Vol. 27, American Astronomical Society Meeting Abstracts, p. 1444
Brunetti G., 2016, Plasma Phys. Control. Fusion, 58, 14011
Brunetti G., Jones T., 2014, IJMPD, 23, 30007
Brunetti G., Lazarian A., 2011, MNRAS, 410, 127
Brunetti G., Lazarian A., 2016, MNRAS, 458, 2584
Brunetti G., Setti G., Feretti L., Giovannini G., 2001, MNRAS, 320, 365
Brunetti G., Venturi T., Dallacasa D., Cassano R., Dolag K., Giacintucci S., Setti G., 2007, ApJ, 670, L5
Brunetti G., Zimmer S., Zandanel F., 2017, MNRAS, 472, 1506
Buote D., 2001, ApJ, 553, L15
Caglar T., 2018, MNRAS, 475, 2870
Caglar T., Hudaverdi M., 2017, MNRAS, 472, 2633
Cash W., 1979, ApJ, 228, 939
Cassano R., Brunetti G., Röttgering H., Brüggen M., 2010a, A&A, 509, A68
Cassano R. et al., 2013, ApJ, 777, 141
Cassano R., Ettori S., Giacintucci S., Brunetti G., Markevitch M., Venturi T., Gitti M., 2010b, ApJ, 721, L82

Chandra P., Ray A., Bhatnagar S., 2004, ApJ, 612, 974

Condon J., Cotton W., Greisen E., Yin Q., Perley R., Taylor G., Broderick J., 1998, AJ, 115, 1693

Cornwell T., Golap K., Bhatnagar S., 2005, in Astronomical Society of the Pacific Conference Series, Vol. 347, Astronomical Data Analysis Software and Systems XIV, Shopbell P., Britton M., Ebert R., eds., p. 86

Cuciti V., Cassano R., Brunetti G., Dallacasa D., Kale R., Ettori S., Venturi T., 2015, A&A, 580, A97

Dahle H., Kaiser N., Irgens R., Lilje P., Maddox S., 2002, ApJS, 139, 313

David L., Kempner J., 2004, ApJ, 613, 831

de Gasperin F. et al., 2017, Science Adv., 3, e1701634

Drabent A., 2017, PhD thesis, Friedrich-Schiller-Universität Jena

Enßlin T., Biermann P., Klein U., Kohle S., Biermann P., Klein U., Kohle S., 1998, A&A, 332, 395

Feretti L., Giovannini G., Govoni F., Murgia M., 2012, A&A Rev., 20, 54

Gastaldello F., Ettori S., Molendi S., Bardelli S., Venturi T., Zucca E., 2003, A&A, 411, 21

Giovannini G., Bonafede A., Feretti L., Govoni F., Murgia M., Ferrari F., Monti G., 2009, A&A, 507, 1257

Guo X., Sironi L., Narayan R., 2014a, ApJ, 794, 153

Guo X., Sironi L., Narayan R., 2014b, ApJ, 797, 47

Gutierrez K., Krawczynski H., 2005, ApJ, 619, 161

Ha J.-H., Ryu D., Kang H., 2018, ApJ, 857, 26

Haines C. et al., 2017, ArXiv e-prints

Haines C., Smith G., Egami E., Okabe N., Takada M., Ellis R., Moran S., Umetsu K., 2009, MNRAS, 396, 1297

Hardcastle M. et al., 2016, MNRAS, 462, 1910

Hoang D. et al., 2017, MNRAS, 471, 1107

Hoeft M., Brüggen M., 2007, MNRAS, 375, 77

Intema H., Jagannathan P., Mooley K., Frail D., 2017, A&A, 598, A78

Intema H., van der Tol S., Cotton W., Cohen A., van Bemmel I., Röttgering H., 2009, A&A, 501, 1185

Kalberla P., Burton W., Hartmann D., Arnal E., Bajaja E., Morras R., Pöppel W., 2005, A&A, 440, 775

Kang H., Petrosian V., Ryu D., Jones T., 2014, ApJ, 788, 142

Kang H., Ryu D., 2011, ApJ, 734, 18

Kang H., Ryu D., 2016, ApJ, 823, 13

Kang H., Ryu D., Jones T., 2012, ApJ, 756, 97

Kato Y., Nakazawa K., Gu L., Akahori T., Takizawa M., Fujita Y., Makishima K., 2015, PASJ, 67, 71

Kempner J., Sarazin C., 2001, ApJ, 548, 639

Keshet U., Waxman E., Loeb A., 2004, ApJ, 617, 281

Lakhchaura K., Singh K., Saikia D., Hunstead R., 2011, ApJ, 743, 78

Landau L., Lifshitz E., 1959, Fluid mechanics

Lane W., Cotton W., van Velzen S., Clarke T., Kassim N., Helmboldt J., Lazio T., Cohen A., 2014, MNRAS, 440, 327

Macario G., Markevitch M., Giacintucci S., Brunetti G., Venturi T., Murray S., 2011, ApJ, 728, 82

Machado R., Monteiro-Oliveira R., Lima Neto G., Cypriano E., 2015, MNRAS, 451, 3309

Markevitch M., Vikhlinin A., 2007, Phys. Rep., 443, 1

Martino R., Mazzotta P., Bourdin H., Smith G., Bartalucci I., Marrone D., Finoguenov A., Okabe N., 2014, MNRAS, 443, 2342

Mazzotta P., Rasia E., Moscardini L., Tormen G., 2004, MNRAS, 354, 10

McMullin J., Waters B., Schiebel D., Young W., Golap K., 2007, in Astronomical Society of the Pacific Conference Series, Vol. 376, Astronomical Data Analysis Software and Systems XVI, Shaw R., Hill F., Bell D., eds., p. 127

Mitsuishi I. et al., 2012, PASJ, 64, 18

Mohan N., Rafferty D., 2015, PyBDSF: Python Blob Detection and Source Finder. Astrophysics Source Code Library

Molnar S., Chiu I.-N., Broadhurst T., Stadel J., 2013, ApJ, 779, 63

Monteiro-Oliveira R., Cypriano E., Machado R., Lima Neto G., Ribeiro A., Sodré L., Dupke R., 2017, MNRAS, 466, 2614

Motl P., Hallman E., Burns J., Norman M., 2005, ApJ, 623, L63

Murgia M., Govoni F., Feretti L., Giovannini G., 2010, A&A, 509, A86

Nagai D., 2006, ApJ, 650, 538

Nuza S., Hoeft M., van Weeren R., Gottlöber S., Yepes G., 2012, MNRAS, 420, 2006

O'Dea C., Owen F., 1985, AJ, 90, 927

Offringa A. et al., 2014, MNRAS, 444, 606

Okabe N., Umetsu K., 2008, PASJ, 60, 345

Paterno-Mahler R., Randall S., Bulbul E., Andrade-Santos F., Blanton E., Jones C., Murray S., Johnson R., 2014, ApJ, 791, 104

Perley R., Butler B., 2013, ApJS, 204, 19

Petrosian V., 2001, ApJ, 557, 560

Pinzke A., Oh S., Pfrommer C., 2013, MNRAS, 435, 1061

Pinzke A., Oh S., Pfrommer C., 2017, MNRAS, 465, 4800

Planck Collaboration VIII, 2013, A&A, 550, A134

Ragozzine B., Clowe D., Markevitch M., Gonzalez A., Bradač M., 2012, ApJ, 744, 94

Rau U., Cornwell T., 2011, A&A, 532, A71

Rengelink R., Tang Y., de Bruyn A., Miley G., Bremer M., Roettgering H., Bremer M., 1997, A&AS, 124

Ricker P., Sarazin C., 2001, ApJ, 561, 621

Ritchie B., Thomas P., 2002, MNRAS, 329, 675

Rizza E., Burns J., Ledlow M., Owen F., Voges W., Bliton M., 1998, MNRAS, 301, 328

Roettiger K., Burns J., Stone J., 1999, ApJ, 518, 603

Roettiger K., Loken C., Burns J., 1997, A&AS, 109, 307

Röttgering H. et al., 2011, J. Astrophys. Astron., 32, 557

Röttgering H. et al., 2006, ArXiv e-prints

Sanders J., 2006, MNRAS, 371, 829

Savini F. et al., 2018, MNRAS, 474, 5023

Scaife A., Heald G., 2012, MNRAS, 423, L30

Shimwell T. et al., 2016, MNRAS, 459, 277

Shimwell T., Markevitch M., Brown S., Feretti L., Gaensler B., Johnston-Hollitt M., Lage C., Srinivasan R., 2015, MNRAS, 449, 1486

Shimwell T. et al., 2017, A&A, 598, A104

Sirothia S., 2009, MNRAS, 398, 853

Takizawa M., 1999, ApJ, 520, 514

Tasse C., van der Tol S., van Zwieten J., van Diepen G., Bhatnagar S., 2013, A&A, 553, A105

van Haarlem M. et al., 2013, A&A, 556, A2

van Weeren R. et al., 2017, Nature Astron., 1, 5

van Weeren R. et al., 2016a, ApJ, 818, 204
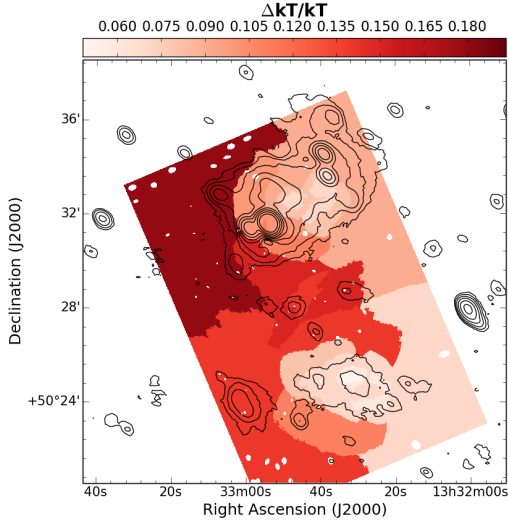
van Weeren R. et al., 2016b, ApJS, 223, 2

Figure A1. Temperature error map of A1758 (cf. with Fig 8).

Vazza F., Brüggen M., 2014, MNRAS, 437, 2291

Vazza F., Brüggen M., Wittor D., Gheller C., Eckert D., Stubbe M., 2016, MNRAS, 459, 70

Vazza F., Eckert D., Brüggen M., Huber B., 2015a, MNRAS, 451, 2198

Vazza F., Ferrari C., Brüggen M., Bonafede A., Gheller C., Wang P., 2015b, A&A, 580, A119

Venturi T., Giacintucci S., Dallacasa D., Cassano R., Brunetti G., Bardelli S., Setti G., 2008, A&A, 484, 327

Venturi T., Giacintucci S., Dallacasa D., Cassano R., Brunetti G., Macario G., Athreya R., 2013, A&A, 551, A24

Wegner G. et al., 2017, ApJ, 844, 67

Wilber A. et al., 2018, MNRAS, 473, 3536

Williams W. et al., 2016, MNRAS, 460, 2385

Wittor D., Vazza F., Brüggen M., 2017, MNRAS, 464, 4448

APPENDIX A: TEMPERATURE MAP

The fractional errors on the temperature map of Fig 8 are reported in Fig. A1. Projected pressure and entropy have similar fractional errors due to their linear dependence on the temperature and to the general small error on the emission measure.

The high value of temperature in the putative post-shock region of Fig. 9 can not be identified in the temperature map of Fig. 8 (left panel) likely due to the fact that the spectral extracting sectors are large, hence they might contain a mix of plasma with different temperatures. In Fig. A2 we show that if the required S/N per region is reduced to 30, the CONTBIN algorithm is able to draw a smaller sector similar in size and position to region 2 in Fig. 9 where the spectral fit provides again $kT \sim 15$ keV, canceling the apparent tension between the two results.

APPENDIX B: X-RAY CHANNEL SPECTRA

The best-fitting spectra of the five regions shown in Fig. 9 are reported in Fig. B1. The spectral model components

Table B1. Impact of the systematic uncertainties of the background modeling on the temperature estimates reported in Fig. 9 (right panel). Tests were performed varying within $\pm 1\sigma$ the normalization level of the instrumental background ("NXB") and of the astrophysical background ("sky"). Temperatures are reported in keV units.

Region	Best fit	NXB		NXB + Sky	
		$+1\sigma$	-1σ	$+1\sigma$	-1σ
1	$4.4^{+2.8}_{-1.4}$	$3.7^{+2.1}_{-1.0}$	$5.4^{+4.1}_{-1.9}$	$3.5^{+4.1}_{-1.5}$	$5.1^{+3.4}_{-1.1}$
2	$15.4^{+9.3}_{-4.8}$	$14.1^{+7.7}_{-3.8}$	$17.1^{+12.5}_{-5.1}$	$15.4^{+9.8}_{-5.1}$	$16.7^{+10.0}_{-5.1}$
3	$12.2^{+3.9}_{-3.6}$	$10.2^{+4.5}_{-2.3}$	$13.6^{+3.5}_{-3.9}$	$11.8^{+4.1}_{-3.4}$	$13.2^{+3.5}_{-3.7}$
4	$5.0^{+1.4}_{-0.9}$	$4.5^{+1.2}_{-0.7}$	$5.4^{+1.5}_{-1.1}$	$4.8^{+1.4}_{-0.9}$	$5.3^{+1.5}_{-1.0}$
5	$2.5^{+0.7}_{-0.5}$	$2.2^{+0.6}_{-0.3}$	$2.7^{+0.9}_{-0.5}$	$2.3^{+0.7}_{-0.4}$	$2.8^{+0.8}_{-0.6}$

are depicted with different colors in the plots. To asses the impact of the systematic uncertainties of the background modeling to the estimates of the ICM temperature, we re-performed the spectral fits varying within $\pm 1\sigma$ the normalization levels first of the instrumental background alone, and later of both the instrumental and astrophysical backgrounds. The results are summarized in Tab. B1 and are consistent within 1σ with that reported in Fig. 9 (right panel). Finally, we mention that the drop of the *Chandra* effective area above 5 keV makes the estimation of high temperatures critical with this instrument. In this respect, the errors on the high temperatures reported in Tab. B1 may not reflect entirely the real range of statistical and systematic uncertainties.

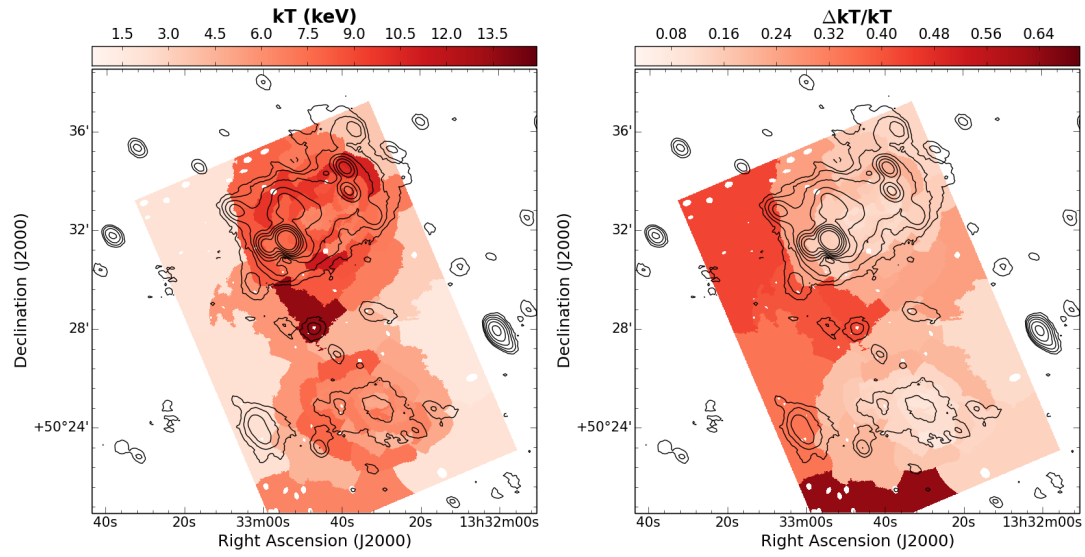This paper has been typeset from a TEX/ LATEX file prepared by the author.

Figure A2. Low S/N temperature map (*left*) and relative error map (*right*) of A1758.
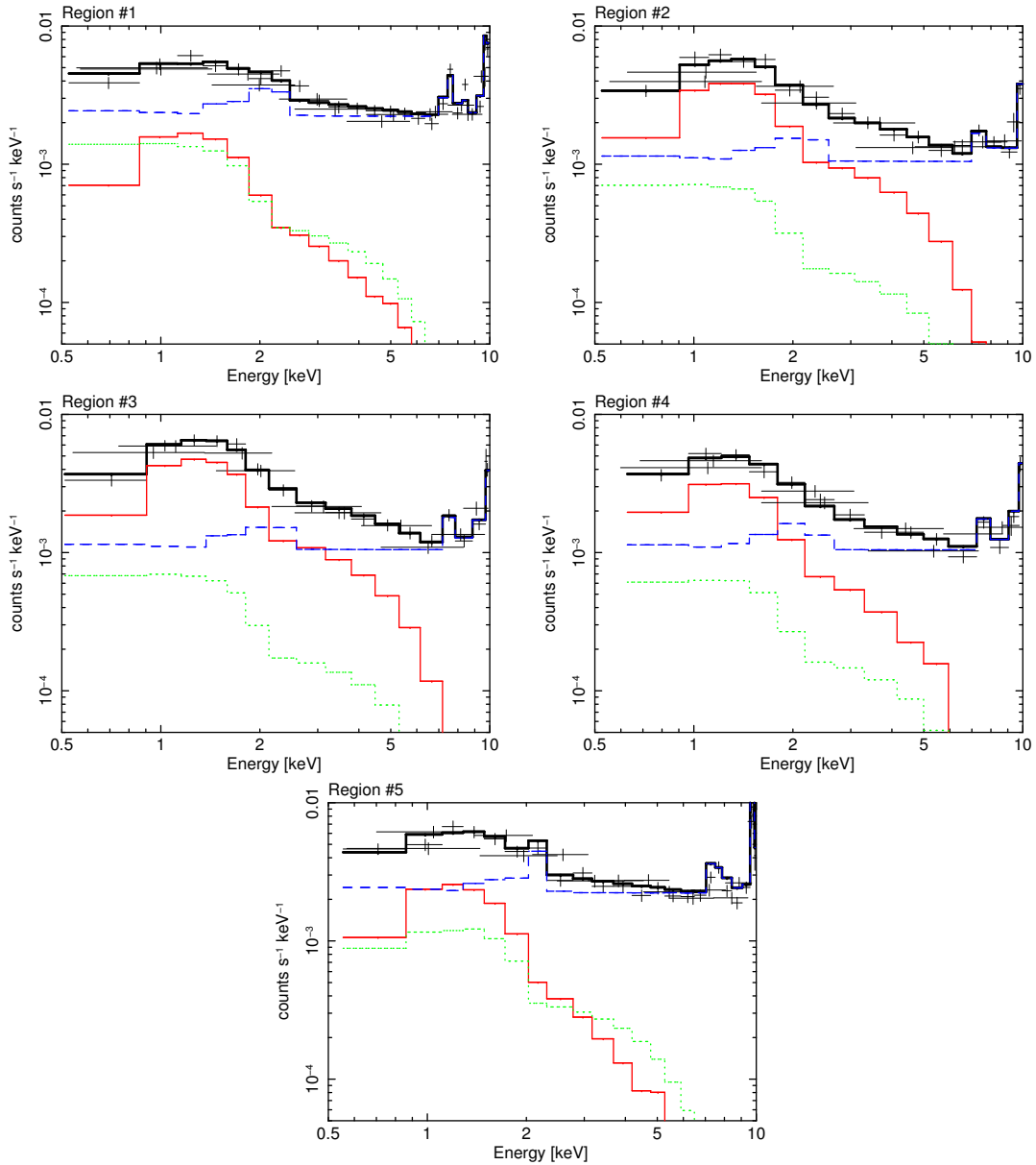
Figure B1. Spectral fitting results for the five regions shown in Fig. 9 (left panel). Data points are shown in black together with the best-fitting model. Different colors denote the components of the spectral model; i.e., the cluster emission (in solid red), the astrophysical background (in dotted green) and the instrumental background (in dashed blue). Whilst the three ObsID spectra were simultaneously fitted, the models for only one observation were reported in order to avoid confusion in the plot. The c-stat/d.o.f. of the fits from region 1 to 5 are: 232/184, 135/127, 114/132, 115/113 and 224/182.